Mode-Voltage Constrained Control for Adaptive Optics System

Ruitao Wang, Youming Guo, Nanfei Yan, Ying Yang, Lanqiang Zhang, Qiong Tu, Lingxiao Li, and Changhui Rao

***Abstract*—In the adaptive optics system of astronomical observation, the deformable mirror and the tip/tilt mirror are coupled during the correction process. However, due to the limited sensitivity of the Shack-Hartmann wavefront sensor in detecting piston aberration, it becomes necessary to constrain piston aberration caused by the deformable mirror. This paper introduces a straightforward and efficient decoupling control algorithm that is based on mode-voltage constraints. The proposed algorithm utilizes the mode method to decompose the control voltage mode, constructs a transition matrix to avoid piston and tip/tilt aberrations, and combines this matrix with the response matrix of the deformable mirror to generate a new reconstruction matrix. The direct slope algorithm is used to obtain the mode coefficient of the control voltage, which is then followed by obtaining the constrained control voltage through the proportional-integral controller and transition matrix. Simulation results demonstrate that this algorithm outperforms both the traditional vector project-constraint algorithm and the projection-based decoupling algorithm. The experimental results demonstrate the effective suppression of coupling between the deformable mirror and tip/tilt mirror by this algorithm, leading to a higher Strehl Ratio and improved correction for first 44-order Zernike mode aberrations.**

***Index Terms*—Deformable mirror, decoupling control algorithm, adaptive optics system.**

I. Introduction

As A core phase-conjugation device, deformable mirror (DM) has found extensive applications in various adaptive optics systems, such as multi-conjugate adaptive optics, ground-layer adaptive optics, single conjugate adaptive optics, multi-target adaptive optics and laser guide star adaptive optics [1], [2], [3], [4], [5]. Recently, our team has successfully developed and installed a high-order piezoelectric deformable secondary mirror on the 1.8-meter telescope at Lijiang Observatory in China, yielding exceptional observation results [6]. The combination of a tip/tilt mirror (TM) and a DM is commonly utilized in the field of astronomical observation to simultaneously correct overall tip/tilt and high-order aberration [7]. The tip/tilt aberration is corrected by the TM, whereas the DM is responsible for correcting high-order aberrations. However, the DM forms tip/tilt aberration during the correction process, which is then compensated for by the TM, establishing a coupling between the two mirrors. Failure to effectively constrain the coupling error can lead to DM producing contrasting surface shapes and gradually reaching saturation over time, resulting in significant stroke wastage and hindering the achievement of anticipated high correction qualities. To prevent this coupling, it is necessary for the DM to avoid forming any tip/tilt aberration. Moreover, considering that the Shack-Hartmann wavefront sensor (WFS) is not sensitive to piston aberration detection, it is crucial for the DM to avoid forming piston aberration in order to optimize actuator stroke utilization and preserve the system's ability to correct high-order aberrations.

The constraint method for generating specific aberrations of DM was enhanced by proposing a Zernike mode based on the algorithm of adding a limitative aberration vector in [8]. The principle involves incorporating a limitative aberration vector into the slope response matrix. Simulation results demonstrate that DM can effectively correct specific aberrations. However, the dynamic characteristics and correction errors in closed-loop control systems have not been thoroughly investigated in [8]. The construction of the coupling matrix increases the number of conditions for the matrix, and when combined with the integration of the control vector of the DM, it weakens the coupling inhibition between two mirrors, ultimately impacting the system's ability to correct aberrations. The vector project-constraint algorithm proposed in [9] eliminates the voltage in the constraint vector space from the control voltage after closed-loop control. The constraint DM only corrects high-order aberrations. However, due to the coupling of the influence function of the DM, there exists a certain error in the control voltage obtained through direct slope algorithm. This error accumulates after integration and

Manuscript received 29 March 2024; revised 16 May 2024; accepted 20 May 2024. Date of publication 23 May 2024; date of current version 5 June 2024. This work was supported in part by the National Natural Science Foundation of China (NSFC) under Grant 12173041 and in part by Youth Innovation Promotion Association, Chinese Academy of Sciences, under Grant 2020376. *(Corresponding author: Youming Guo.)*

Ruitao Wang, Youming Guo, Nanfei Yan, Ying Yang, Lanqiang Zhang, and Changhui Rao are with the National Laboratory on Adaptive Optics, Chengdu 610209, China, also with the Key Laboratory on Adaptive Optics, Chinese Academy of Sciences, Chengdu 610209, China, also with the Institute of Optics and Electronics, Chinese Academy of Sciences, Chengdu 610209, China, and also with the University of Chinese Academy of Sciences, Beijing 100049, China (e-mail: 804124514@qq.com; guoyouming@ioe.ac.cn; yannf16@163.com; 565720337@qq.com; lqzhang@ioe.ac.cn; chrao@ioe.ac.c).

Qiong Tu is with the Institute of Optics and Electronics, Chinese Academy of Sciences, Chengdu 610209, China, and also with the University of Chinese Academy of Sciences, Beijing 100049, China (e-mail: 1634102038@qq.com).

Lingxiao Li is with the Key Laboratory on Adaptive Optics, Chinese Academy of Sciences, Chengdu 610209, China, and also with the Institute of Optics and Electronics, Chinese Academy of Sciences, Chengdu 610209, China (e-mail: lilingxiao@ioe.ac.cn).

Digital Object Identifier 10.1109/JPHOT.2024.3404397

prevents complete removal of coupling voltage in the constraint vector space.

Similar to the single DM system, the dual DMs system also encounters the challenge of dealing with coupling between two deformable mirrors. Several dual DMs system control algorithms have been proposed, such as two-step control algorithm [10], [11], [12], Zernike mode decomposition algorithm [8], [13], [14], [15], Fourier mode decomposition algorithm [16], wavelet mode decomposition algorithm [17], Lagrange-multiplier damped least-squares algorithm [18], [19], [20], [21] and projection-based decoupling algorithm [22]. But the algorithm which can effectually suppress the coupling errors between the two DMs is very few. So far, the Zernike mode decomposition algorithm and projection-based decoupling algorithm can get better performance to restrain coupling error between the dual DMs [23]. The key to the Zernike mode decomposition algorithm lies in constructing a coupling suppression matrix. Given the non-orthogonality of Zernike's first-order partial derivatives, it becomes imperative to accurately measure or fit the surface shape of the actuator response function prior to constructing the coupling suppression matrix. For DM with a large number of actuators, this measurement process can become excessively cumbersome. The projection-based decoupling algorithm [22] failed to allocate aberrations of different spatial frequencies reasonably based on the fitting ability of the DM, and it is necessary for the column vectors of the introduced wavefront restoration matrix to possess orthogonality.

In this paper, we propose a mode-voltage constrained control algorithm based on the Zernike mode to address the piston and tip/tilt aberrations caused by DM. The Zernike mode method [24] is employed for decomposing the control voltage into modes, eliminating the mode voltages that introduce piston and tip/tilt aberrations, and constructing a novel restoration matrix while imposing constraints on the number of conditions. The control voltage obtained through the least squares method does not include any constraint terms, and the constraint residuals do not accumulate after passing through the leaky integrator (LI). In Section II, we present this algorithm and conduct an analysis of the error associated with the traditional vector project-constraint algorithm [9]. Section III provides a brief description of the DM and experimental platform used. The simulation results are presented in Section IV, followed by the experimental results in Section V. Finally, conclusions and future work are presented in Section VI.

II. Principles and Analysis of Different Algorithms

A. Mode-Voltage Constrained Control Algorithm

The wavefront aberrations to be corrected in a single DM system can be categorized into tip/tilt aberration, which is corrected by TM, and high-order aberration, which is corrected by DM. In the Zernike mode method, the piston aberration can be denoted as Φ_0, while the tip/tilt aberration can be denoted as Φ_1 (x-tilt) and Φ_2 (y-tilt), respectively:

$$\Phi_0 = a_0 \cdot Z_0, \tag{1}$$

$$\Phi_1 = a_1 \cdot Z_1, \tag{2}$$

$$\Phi_2 = a_2 \cdot Z_2, \tag{3}$$

where a_0, a_1 and a_2 are the coefficients of the Zernike polynomial for the zeroth, first, and second terms. Z_0 is the piston term of the Zernike polynomial. Z_1 is the x-tilt term of the Zernike polynomial. Z_2 is the y-tilt term of the Zernike polynomial. The number of active actuators for continuous surface DM is denoted as N. The influence function of the kth active actuator on the surface shape of the DM, typically considered as a Gaussian function [15], is represented by $f_k(x, y)$. The control voltage applied to the kth active actuator is denoted as v_k. Consequently, the wavefront phase reconstructed by the DM can be mathematically expressed:

$$\Phi_3 = \sum_{k=1}^{N} v_k \cdot f_k(x, y). \tag{4}$$

The imposition of constraints on the DM is necessary in order to prevent the occurrence of tip/tilt and piston aberrations. Given that the Zernike polynomial exhibits orthogonality within the unit circle domain, the DM-constrained conditions for the first three orders of Zernike polynomial aberrations Z_i are as follows:

$$\begin{cases} \iint \Phi_0 \Phi_3 dxdy = a_0 \sum_{k=1}^{N} v_k \iint f_k(x, y) dxdy = 0 \\ \iint \Phi_1 \Phi_3 dxdy = a_1 \sum_{k=1}^{N} v_k \iint x f_k(x, y) dxdy = 0 \\ \iint \Phi_2 \Phi_3 dxdy = a_2 \sum_{k=1}^{N} v_k \iint y f_k(x, y) dxdy = 0 \end{cases}, \tag{5}$$

By numerically integrating (5), it can be approximated as:

$$\begin{cases} \sum_{k=1}^{N} v_k = 0 \\ \sum_{k=1}^{N} v_k x_k = 0 \\ \sum_{k=1}^{N} v_k y_k = 0 \end{cases}, \tag{6}$$

The coordinates of the kth active actuator in the x and y directions on the unit circle are represented by x_k and y_k respectively. The given (6) can be transformed into vector form.

$$\begin{cases} \boldsymbol{v} \cdot \boldsymbol{p} = 0 \\ \boldsymbol{v} \cdot \boldsymbol{x} = 0 \\ \boldsymbol{v} \cdot \boldsymbol{y} = 0 \end{cases}, \tag{7}$$

The vectors $\boldsymbol{p}$, $\boldsymbol{x}$ and $\boldsymbol{y}$ are formed by combining elements 1, x_k and y_k respectively. The vector $\boldsymbol{v}$ represents the control voltage of the actuator. The dot product of a vectored is denoted by $\cdot$. Equation (7) indicates that when the constraint of piston and tip/tilt is applied to the DM, the projection of the actual control voltage onto the vectors $\boldsymbol{p}$, $\boldsymbol{x}$ and $\boldsymbol{y}$ should be zero. The constraint vectors are designed to ensure that the DM does not introduce tip/tilt and piston aberrations. The actual voltage control vector v' applied is obtained by removing the projection from the voltage vector.

$$v' = (I - P_x)(I - P_y)(I - P_{piston})v = Mv. \tag{8}$$

The size of the identity matrix I is determined by the number of active actuators, while the projection matrix P_x, P_y and P_{piston} represent the subspace consisting of constraint vectors $\boldsymbol{x}$, $\boldsymbol{y}$, and $\boldsymbol{p}$ respectively. $(I - P_x)(I - P_y)(I - P_{piston})$ in the 8 is represented by M, which is a conversion matrix projecting voltage vector to actual controlled voltage vector, and it should be decomposed into three terms with singular value decomposition

(SVD) method.

$$M = USV^T. \tag{9}$$

The matrix S in (9) is a diagonal matrix containing the singular values of M, while U is a unitary matrix composed of eigenvectors of M. However, considering the constraints imposed on piston and tip/tilt aberrations, the smallest three eigenvalues are disregarded, resulting in the removal of their corresponding column eigenvectors from matrix U.

$$U_1 = \begin{bmatrix} U(1,1) & U(1,2) & \cdots & U(1,N-3) \\ U(2,1) & U(2,2) & \cdots & U(2,N-3) \\ \vdots & \vdots & \cdots & \vdots \\ U(N,1) & U(N,2) & \cdots & U(N,N-3) \end{bmatrix}, \tag{10}$$

$$v' = U_1 e, \tag{11}$$

$$e = U_1^+ v', \tag{12}$$

The transition matrix of the DM in (10) is denoted as U_1 and comprises eigenvectors associated with the mode coefficient. The vector e represents the mode coefficient of DM. By multiplying U_1 with e, DM's actual voltage control vector v' can be obtained. Consequently, by combining the response matrix R of DM with U_1, we can obtain the matrix D for the mode coefficient to slope of the DM.

$$D = RU_1, \tag{13}$$

$$g = RU_1 e = De, \tag{14}$$

$$e = D^+ g. \tag{15}$$

where D^+ is the pseudo-inverse matrix of D. After the wavefront slope g to be corrected is obtained, the mode coefficient vector can be calculated by the LI. And then use the transition matrix U_1 from the mode coefficient vector to the control vector of DM to get the actual voltage control vector $V(k+1)$.

$$a(k+1) = \alpha a(k) + \beta e(k), \tag{16}$$

$$V(k+1) = U_1 a(k+1). \tag{17}$$

The control parameters of LI, denoted as α and β in (16), respectively. In the whole experiment process, the value of α is 0.999 and the value of β is 0.1.

B. Vector Project-Constraint Algorithm and Its Impact on System Performance

According to the description in [9], when the vector project-constraint algorithm [9] is used for real-time restoration calculation, the error voltage of the DM is obtained first by the direct slope algorithm. After closed-loop LI, the error voltage is removed by the projection of the control voltage $V(k+1)$ on the subspace composed of $\boldsymbol{p}$, $\boldsymbol{x}$ and $\boldsymbol{y}$ according to (7), and the projection vectors are respectively:

$$v = R^+ g, \tag{18}$$

$$V(k+1) = \alpha \times V(k) + \beta \times v(k), \tag{19}$$

$$\begin{cases} V_p = \frac{(V(k+1),p)}{(p,p)} p \\ V_x = \frac{(V(k+1),x)}{(x,x)} x \\ V_y = \frac{(V(k+1),y)}{(y,y)} y \end{cases}, \tag{20}$$

In order to prevent the DM from producing tip/tilt and piston aberrations, the actual applied control voltage is constrained, so the actual applied voltage $V'(k+1)$ is obtained by removing the projection from the voltage vector.

$$V'(k+1) = V(k+1) - V_p - V_x - V_y. \tag{21}$$

The restoration algorithm under the least square error, as represented by (15) and (18), aims to minimize the sum of squares between the actual slope measured by WFS and the slope generated by DM restoration in the system.

$$||S_i - S||_2^2 = \sum_{i=1}^{3} S_i^2 + \sum_{i=4}^{n} (S_i - S)^2, \tag{22}$$

The three components of the second part of (22) are

$$\begin{cases} S_1 = \boldsymbol{V} \cdot \boldsymbol{p} \\ S_2 = \boldsymbol{V} \cdot \boldsymbol{x} \\ S_3 = \boldsymbol{V} \cdot \boldsymbol{y} \end{cases}, \tag{23}$$

where S_i represents the slope generated by the DM, S represents the actual detected slope, S_1, S_2, and S_3 represent the projection of the voltage vector $\boldsymbol{V}$ on the $\boldsymbol{p}$, $\boldsymbol{x}$, and $\boldsymbol{y}$ vectors, respectively. The relative magnitudes of these errors reflect the residual error in the DM voltage along the piston, x-tilt, and y-tilt directions. The vector project-constraint algorithm [9] does not impose constraints on the second part of (22) when calculating the error voltage in (18), and WFS is not sensitive to detecting piston aberrations, which can increase the error introduced by the second part of (22) and impact the overall slope of errors. The error voltage obtained from (18) may continue to accumulate to a relatively large value after passing through the LI. Although (21) subtracts the voltage projection vector on piston and tip/tilt aberrations, $V'(k+1)$ at this point is not the optimal control voltage obtained by using least square method, which takes into account the influence of error slope on piston and tip/tilt aberrations. The DM still compensates for a small amount of piston and tip/tilt aberrations, thereby not fully exerting its correction capability.

III. Setup of the Testing Platform

A. Deformable Mirror Used

The DM utilized in the field test was developed by the Institute of Optics and Electronics of the Chinese Academy of Sciences (IOE), with its parameters listed in Table I. This particular DM has demonstrated exceptional performance during calibration procedures for the Educational Adaptive-optics Solar Telescope (EAST) [25]. The AO system, comprising 177 active actuators and 177 effective sub-apertures, monitors the surface contour (shape) of the mirror within a circular mirror area (pupil). The active actuators refer to those located within the designated pupil region. This is a typical practice in DM control [26]. By removing the actuator outside the pupil, the quality and realism

TABLE I
THE PARAMETERS OF THE DM

Parameters	Value
Number of actuator	185
Active actuators	177
Arrangement	Square
Type	Continuous surface DM
Clear aperture of DM	39 mm
Pitch	300 μm
Stroke	$\pm$ 2.6 μm

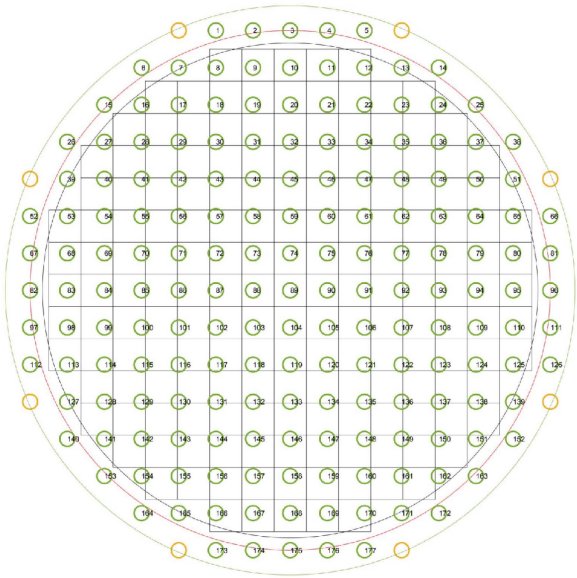

Fig. 1. Configuration of WFS's sub-apertures and DM's actuators.

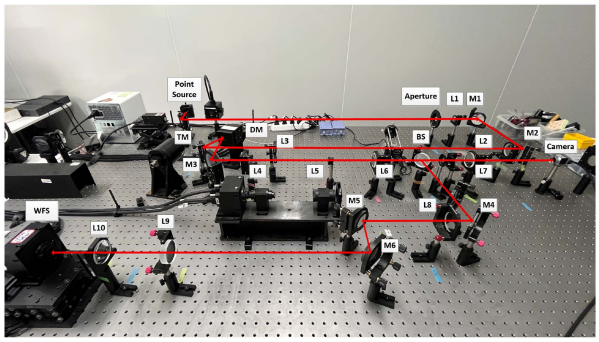

Fig. 2. Optical layout of experimental system (L means lens, M means mirror,and BS is a beam splitter).

of the shape formed inside the pupil can be improved, in addition, the negative effects of edge effects can be reduced. The layout relationship between WFS's sub-apertures and DM's actuators in the system is illustrated in Fig. 1, where squares denote wavefront sensors' sub-aperture positions and small green circles with numbers represent the active actuator arrangement.

B. Experimental Platform

The optical system is depicted in Fig. 2. The point source employs visible light with a wavelength of 650 nm. The light traverses multiple lenses, mirrors, TM and DM, before reaching

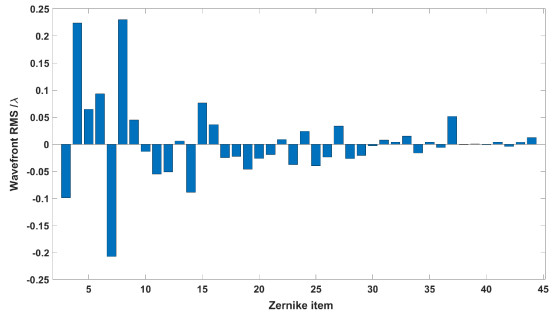

Fig. 3. The first 44-order Zernike coefficients of phase aberration.

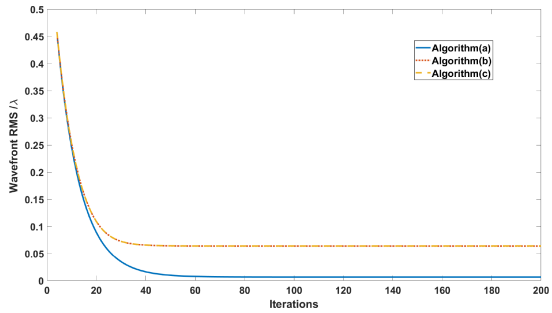

Fig. 4. Aberration RMS curve corrected using three algorithms in simulation.

a beam splitter mirror where half of the light is directed towards the scientific camera and the other half towards the WFS. The clear aperture of WFS measures 630 mm. The microlens array consists of 15 $\times$ 15 elements, with an effective count of 177 microlenses. Each sub-aperture has an edge length of 24 (8 μm) pixels, for a total subaperture array size of 360 $\times$ 360 pixels. Each microlens measures at dimensions of 192 μm 192 μm while possessing a focal length of 7.7 μm. The far field scientific camera employed is acA4024-29um from Basler ace series featuring 12-bit capability. This represents a typical single DM AO system.

IV. NUMERAL SIMULATION

To ensure consistency between simulation and experimental results, it is necessary to maintain consistent simulation parameters for both DM and WFS with those of the actual system. Taking the numerical model consisting of 177 active actuators, 177 active sub-apertures of DM and WFS as an example, a comparative analysis was conducted through simulation to evaluate the correction effects of the aforementioned two algorithms. Additionally, the projection-based decoupling algorithm [22] was also employed in the numerical model. In this simulation, the input wavefront aberration comprised the first 44-order Zernike modes, as depicted in Fig. 3.

The numerical system is controlled by one of the following algorithms: (a) the mode-voltage constrained control algorithm proposed in this paper, (b) vector projection constraint algorithm [9], (c) projection-based decoupling algorithm [22]. Fig. 4 shows the RMS curves of the residual wavefront during the correction process in the simulation. After correction by algorithm (a), the RMS of the residual wavefront is reduced to

TABLE II
VOLTAGE CONSTRAINT ERROR OF DM AT 200TH FRAME IN SIMULATION

Algorithm	S_1	S_2	S_3
Algorithm (a) /V	3.6380e-17	6.4257e-18	-1.6421e-17
Algorithm (b) /V	7.4455	-0.0389	-0.0354
Algorithm (c) /V	4.6504e-15	-0.0346	-0.0371

0.01λ, and when correction is performed by algorithm (b)and (c), the RMS of the residual wavefront is reduced to 0.06λ. The results demonstrate the effective enhancement of DM's correction ability by algorithm (a), while algorithms (b) and (c) exhibit comparable correction performance. Simulation results indicate that, compared to the traditional vector projection constraint algorithm [9] and the projection-based decoupling algorithm [22], the proposed algorithm in this paper achieves superior correction performance.

According to (22), the voltage constraint of the DM after the closed-loop is analyzed. Table II shows the magnitude of the constraint residual of the DM voltage in the piston, x-tilt, and y-tilt directions at the 200th frame. The simulation results demonstrate that the vector projection constraint algorithm [9] effectively enforces the tip/tilt aberration constraint on the control voltage. However, when utilizing the direct slope algorithm, WFS exhibits low sensitivity to piston aberration detection caused by DM, resulting in a significant value for the piston aberration constraint S_1 and incomplete suppression of the constraint term due to integral effects. The projection-based decoupling algorithm [22] effectively constrains the piston and tip/tilt aberrations. Both Fig. 4 and Table II demonstrate that the mode-voltage constrained control algorithm more effectively restricts the generation of piston and tip/tilt aberrations, yielding superior correction results compared to the other two algorithms.

V. EXPERIMENTAL TESTS

The experimental platform established in Section III-B was utilized to validate these three algorithms, showcasing their efficacy within an operational AO system. The three algorithms include: (a) the mode-voltage constrained control algorithm proposed in this paper, (b) the vector projection-constraint algorithm [9], and (c) the projection-based decoupling algorithm [22]. Perform closed-loop control on the previously introduced closed-loop control parameters, limiting the control voltage of the DM to within ± 2 V during the closed-loop process and setting boundary values for any excess.

Before correction, RMS of the wavefront is 0.45λ (λ = 650 nm). The initial aberration is shown in Fig. 5(i). In the experiment, after only using the algorithm (a) proposed in this paper for correction, the RMS of the residual wavefront decreased to 0.02λ, as shown in Fig. 5(ii). After correction by algorithm (b) alone, the RMS of the residual wavefront drops to 0.05λ, as shown in Fig. 5(iii). Finally, the RMS of the residual wavefront is reduced to 0.07λ by using only algorithm (c) for correction, as shown in Fig. 5(iv). Fig. 6 shows the RMS values of residual wavefront errors corrected by three different algorithms in open and closed loop steady states.

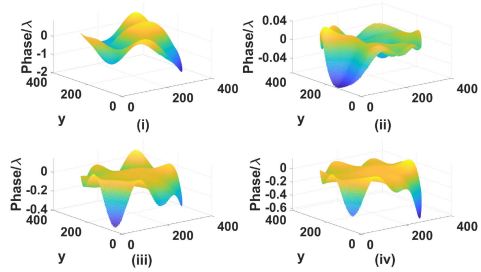

Fig. 5. (i) The initial aberrations (RMS = 0.45λ), (ii) The residual wavefront after correction only by the algorithm (a) (RMS = 0.02λ), (iii) The residual wavefront corrected only by the algorithm (b) (RMS = 0.05λ), (iv) The residual wavefront corrected only by the algorithm (c) (RMS = 0.07λ).

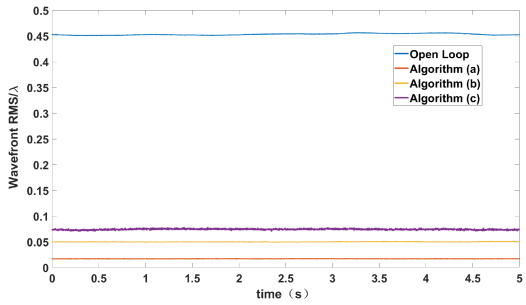

Fig. 6. RMS of residual wavefront corrected by three algorithms.

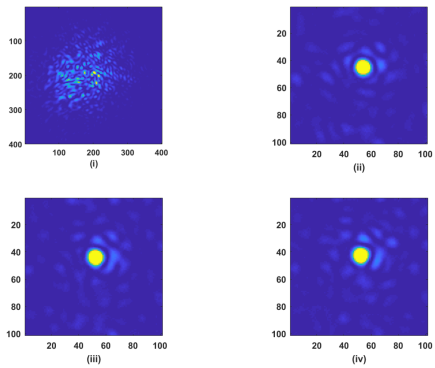

Fig. 7. (i) Open loop far-field spot, (ii) Algorithm (a) corrected far-field image, (ii) Algorithm (b) corrected far-field image, (iv) Algorithm (c) corrected far-field image.

The far-field spot image in the open loop state is depicted in Fig. 7(i). Subsequently, employing algorithm (a) to stabilize the closed loop yields the far-field image shown in Fig. 7(ii). Following closed-loop correction using algorithm (b), the resulting far-field image is presented in Fig. 7(iii). Finally, after implementing algorithm (c) for correction, the corresponding far-field image is displayed in Fig. 7(iv).

The Strehl Ratio (SR) is used as the evaluation indicator, which represents the ratio of the peak value of the far-field image after closed-loop to that without aberration [27]. Both the mode-voltage constrained control algorithm and vector projection constraint algorithm [9] exhibit stable SR after closed-loop. Fig. 8 demonstrates the correction ability of different algorithms, revealing that the proposed mode-voltage constrained control algorithm achieves better correction effect compared to traditional vector projection constraint algorithm [9] and projection-based

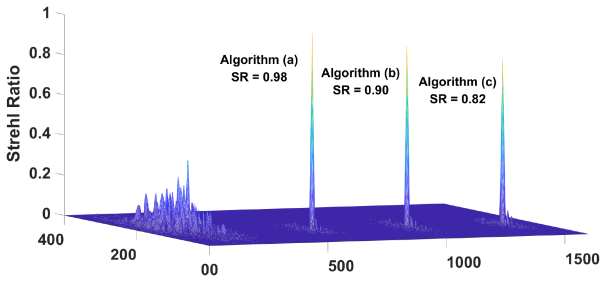

Fig. 8. Comparison of correction ability of different algorithms.

TABLE III
VOLTAGE CONSTRAINT ERROR OF DM AT 200TH FRAME

Algorithm	S_1	S_2	S_3
Algorithm (a) /V	1.0762e-5	-1.6420e-4	-1.0252e-4
Algorithm (b) /V	0.0424	-0.0078	0.0075
Algorithm (c) /V	0.0577	-0.0079	-0.0061

decoupling algorithm [22]. Table III illustrates that in actual AO systems, the mode-voltage constrained control algorithm exhibits a smaller constraint residual for constraint terms. A small amount of constraint residual is attributed to voltage saturation and voltage limiting.

VI. CONCLUSION

This paper proposes and discusses a simple and effective control algorithm based on mode-voltage constraints for the voltage limitations of DM in closed-loop control of AO systems. This algorithm not only eliminates the accumulation of coupling errors between the TM and the DM, but also restricts the DM from producing piston aberration to prevent wasteful actuator stroke, thereby significantly enhancing its correction capability. The simulation results demonstrate that this algorithm outperforms traditional vector project-constraint algorithms and projection-based decoupling algorithms. A typical single DM AO system was established to validate the effectiveness of the proposed algorithm. The experimental results indicate that the AO system controlled by this algorithm effectively mitigates coupling issues between two mirrors and achieves long-term stability with ease. In future applications, this algorithm can be further extended to double deformable mirrors AO systems to enhance image aberration correction for high-spatial resolution telescopes.

REFERENCES

[1] M. Langlois, G. Moretto, K. Richards, S. Hegwer, and T. R. Rimmele, "Solar multiconjugate adaptive optics at the DUNN solar telescope: Preliminary results," *Proc. SPIE*, vol. 5490, pp. 59–66, 2004.
[2] T. Travouillon, J. S. Lawrence, and L. Jolissaint, "Ground layer adaptive optics performance in Antarctica," *Proc. SPIE*, vol. 5490, pp. 934–942, 2004.
[3] G. Sivo, C. Kulcsár, J. M. Conan, H. F. Raynaud, and A. Longmore, "First on-sky SCAO validation of full LQG control with vibration mitigation on the canary pathfinder," *Opt. Exp.*, vol. 22, no. 19, pp. 23565–23591, 2014.
[4] Y. Guo et al., "Adaptive optics based on machine learning: A review," *Opto-Electron. Adv.*, vol. 5, no. 7, 2022, Art. no. 200082.
[5] R.-T. Wang et al., "First sodium laser guide star asterism launching platform in China on the 1.8 m telescope at Gaomeigu observatory," *Astronomical Soc. Pacific*, vol. 135, 2023, Art. no. 034502.
[6] Y. Guo et al., "High-resolution visible imaging with piezoelectric deformable secondary mirror: Experimental results at the 1.8-m adaptive telescope," *Opto-Electron. Adv.*, vol. 6, no. 12, 2023, Art. no. 230039. [Online]. Available: https://www.researching.cn/articles/OJe95dd5d32bdcd061
[7] F. Roddier and L. Thompson, "Adaptive optics in astronomy," *Phys. Today*, vol. 53, no. 4, p. 69, 2000.
[8] S. Hu, B. Xu, X. Zhang, J. Hou, J. Wu, and W. Jiang, "Double-deformable-mirror adaptive optics system for phase compensation," *Appl. Opt.*, vol. 45, no. 12, pp. 2638–2642, Apr. 2006. [Online]. Available: https://opg.optica.org/ao/abstract.cfm?URI=ao-45-12-2638
[9] C. Shanqiu, L. Wenjin, D. Lizhi, W. Shuai, and Y. Yutang, "Constraint study on deformable mirror in close-loop adaptive optics system," *Acta Optica Sinica*, vol. 35, no. 12, 2015, Art. no. 1201002.
[10] D. C. Chen, S. M. Jones, and S. S. Olivier, "High-resolution adaptive optics scanning laser ophthalmoscope with dual deformable mirrors for large aberration correction," *Int. Soc. Opt. Photon.*, 2007.
[11] R. Zawadzki, S. S. Choi, S. M. Jones, S. S. Oliver, and J. S. Werner, "Adaptive optics-optical coherence tomography: Optimizing visualization of microscopic retinal structures in three dimensions," *J. Opt. Soc. Amer.*, vol. 24, no. 5, pp. 1373–1383, 2007.
[12] B. Cense et al., "Volumetric retinal imaging with ultrahigh-resolution spectral-domain optical coherence tomography and adaptive optics using two broadband light sources," *Opt. Exp.*, vol. 17, no. 5, pp. 4095–4111, 2009.
[13] X. Lei et al., "Double-deformable-mirror adaptive optics system for laser beam cleanup using blind optimization," *Opt. Exp.*, vol. 20, no. 20, pp. 22143–22157, 2012.
[14] L. Chaohong et al., "A correction algorithm to simultaneously control dual deformable mirrors in a woofer-tweeter adaptive optics system," *Opt. Exp.*, vol. 18, no. 16, pp. 16671–16684, 2010.
[15] W. Liu et al., "A Zernike mode decomposition decoupling control algorithm for dual deformable mirrors adaptive optics system," *Opt. Exp.*, vol. 21, no. 20, pp. 23885–23895, 2013.
[16] J. F. Lavigne and J.-P. Véran, "Woofer-tweeter control in an adaptive optics system using a fourier reconstructor," *J. Opt. Soc. Amer. A*, vol. 25, no. 9, pp. 2271–2279, 2008.
[17] P. J. Hampton, P. Agathoklis, R. Conan, and C. Bradley, "Closed-loop control of a Woofer–Tweeter adaptive optics system using wavelet-based phase reconstruction," *J. Opt. Soc. Amer.*, vol. 27, no. 11, pp. A145–A156, Nov. 2010. [Online]. Available: https://opg.optica.org/josaa/abstract.cfm?URI=josaa-27-11-A145
[18] W. Zou, X. Qi, and S. A. Burns, "Wavefront-aberration sorting and correction for a dual-deformable-mirror adaptive-optics system," *Opt. Lett.*, vol. 33, no. 22, pp. 2602–2604, Nov. 2008. [Online]. Available: https://opg.optica.org/ol/abstract.cfm?URI=ol-33-22-2602
[19] W. Zou and S. A. Burns, "High-accuracy wavefront control for retinal imaging with adaptive-influence-matrix adaptive optics," *Opt. Exp.*, vol. 17, pp. 20167–20177, 2009.
[20] W. Zou, X. Qi, and S. A. Burns, "Woofer-tweeter adaptive optics scanning laser ophthalmoscopic imaging based on lagrange-multiplier damped least-squares algorithm," *Biomed. Opt. Exp.*, vol. 2, no. 7, pp. 1986–2004, 2011.
[21] W. Zou and S. A. Burns, "Testing of Lagrange multiplier damped least-squares control algorithm for woofer-tweeter adaptive optics," *Appl. Opt.*, vol. 51, no. 9, pp. 1198–1208, 2012.
[22] T. Cheng et al., "Projection-based decoupling algorithm for a woofer-tweeter adaptive optics system," *Proc. SPIE*, vol. 57, no. 6, 2018, Art. no. 065101.
[23] T. Cheng, W. Liu, B. Pang, P. Yang, and B. Xu, "A slope-based decoupling algorithm to simultaneously control dual deformable mirrors in a woofer-tweeter adaptive optics system," *Chin. Phys. B*, vol. 27, no. 7, pp. 279–288, 2018.
[24] G. Youming, W. Yu, L. Ying, R. Xuejun, and R. Changhui, "val for astronomical Shack–Hartmann wavefront sensors," *Monthly Notices Roy. Astronomical Soc.*, vol. 3, p. 3, 2021.
[25] C. Rao et al., "East-educational adaptive-optics solar telescope," *Res. Astron. Astrophys.*, vol. 22, 2022, Art. no. 065003.
[26] A. Haber and T. Bifano, "General approach to precise deformable mirror control," *Opt. Exp.*, vol. 29, no. 21, pp. 33741–33759, Oct. 2021. [Online]. Available: https://opg.optica.org/oe/abstract.cfm?URI=oe-29-21-33741
[27] N. Jovanovic et al., "Demonstration of an efficient, photonic-based astronomical spectrograph on an 8-m telescope," *Opt. Exp.*, vol. 25, no. 15, pp. 17753–17766, 2017.